The Astrophysical Journal, 836:19 (14pp), 2017 February 10 doi:10.3847/1538-4357/836/1/19

Properties of Dense Cores Embedded in Musca Derived from Extinction Maps and ^{13}CO, $C^{18}O$, and NH_3 Emission Lines

Dinelsa A. Machaieie[1,2], José W. Vilas-Boas[1], Carlos A. Wuensche[1], Germán A. Racca[3], Philip C. Myers[4], and Gabriel R. Hickel[5]
[1] Instituto Nacional de Pesquisas Espaciais, Av. dos Astronautas 1.758—Jardim da Granja, CEP-12227-010, São José dos Campos, SP, Brasil; dinelsa.machaieie@inpe.br
[2] Universidade Eduardo Mondlane, Faculdade de Ciências, Departamento de Física, Av. Julius Nyerere-Campus Universitário, C.P. 254, Maputo, Mozambique
[3] Universidade do Estado do Rio Grande do Norte, Faculdade de Ciências Exatas e Naturais/Depto. de Física, Campus Universitário Central, Setor II BR 110, KM 48, Rua Prof. António Campos, Costa e Silva 59610-090—Mossoró-RN, Brazil
[4] Harvard-Smithsonian Center for Astrophysics, 60 Garden Street, Cambridge, MA 02138, USA
[5] Universidade Federal de Itajubá, Departamento de Física, Av. BPS, 1303, Pinheirinho, Itajubá, MG, Brazil
Received 2016 June 20; revised 2016 December 2; accepted 2017 January 2; published 2017 February 6

Abstract

Using near-infrared data from the Two Micron All Sky Survey catalog and the Near Infrared Color Excess method, we studied the extinction distribution in five dense cores of Musca, which show visual extinction greater than 10 mag and are potential sites of star formation. We analyzed the stability in four of them, fitting their radial extinction profiles with Bonnor–Ebert isothermal spheres, and explored their properties using the $J = 1$–0 transition of ^{13}CO and $C^{18}O$ and the $J = K = 1$ transition of NH_3. One core is not well described by the model. The stability parameter of the fitted cores ranges from 4.5 to 5.7 and suggests that all cores are stable, including Mu13, which harbors one young stellar object (YSO), the IRAS 12322-7023 source. However, the analysis of the physical parameters shows that Mu13 tends to have larger A_V, n_c, and P_{ext} than the remaining starless cores. The other physical parameters do not show any trend. It is possible that those are the main parameters to explore in active star-forming cores. Mu13 also shows the most intense emission of NH_3. Its ^{13}CO and $C^{18}O$ lines have double peaks, whose integrated intensity maps suggest that they are due to the superposition of clouds with different radial velocities seen in the line of sight. It is not possible to state whether these clouds are colliding and inducing star formation or are related to a physical process associated with the formation of the YSO.

Key words: dust, extinction – ISM: kinematics and dynamics – ISM: molecules – radio lines: ISM

1. Introduction

Low-mass stars are born within dense cores (with densities higher than $10^4\,cm^{-3}$; Myers 1999; Lada et al. 2010) embedded in globules owing to gravitational instability (Larson 2003). In order to understand how cores evolve into stars, it is necessary to probe the gas properties of their parental molecular clouds, which are mostly determined from observations of rotational lines of molecular tracers such as CO, NH_3, H_2CO, N_2H^+, and others (Myers & Benson 1983; van Dishoeck et al. 1995; Vilas-Boas et al. 2000; Bergin et al. 2001; Caselli et al. 2002; Tafalla et al. 2004).

The results derived from molecular tracers can be complemented by measurements of the visual extinction of background starlight produced at optical (Dickman 1978a) and near-infrared (NIR) wavelengths (Lada et al. 1994), assuming a constant gas-to-dust ratio (Bohlin et al. 1978; Vuong et al. 2003; Liszt 2014). However, techniques using optical star counts probe the regions with visual extinction smaller than 8 mag only (Cernicharo & Bachiller 1984; Andreazza & Vilas-Boas 1996; Cambrésy 1999), while from NIR color excess it is possible to reach regions with $A_V \sim 40$ mag (Kandori et al. 2005). The NIR color excess approach also produces detailed extinction maps and provides information on physical structure of globules, at early stages of star formation, including their stability (Alves et al. 2001; Harvey et al. 2001; Racca et al. 2002, 2009; Kandori et al. 2005; Teixeira et al. 2005; Huard et al. 2006). Although Musca is one of the nearest clouds, located at a distance of 150 pc (Arnal et al. 1993; Corradi et al. 1997; Knude & Hog 1998), none of its globules have their stability analyzed.

Musca is a filamentary dark cloud, with ~6.5 pc length and ~0.5 pc width (Gregorio Hetem et al. 1988; Pereyra & Magalhães 2004), located at the northern end of the Chamaeleon–Musca complex (Feitzinger & Stuewe 1984; Franco 1991). All condensations (regions defined by the contour of visual extinction greater than 5 mag) of Musca lie approximately along the same line in the plane of the sky. The condensation designated as Mu13 by Vilas-Boas et al. (1994), located at the northern end of the cloud, harbors one young stellar object (YSO), the IRAS 12322-7023 source, classified as a probable T-Tauri-like star (Gregorio Hetem et al. 1988). The remaining condensations are starless.

Polarimetry studies (Arnal et al. 1993; Pereyra & Magalhães 2004) found the overall magnetic field in the neighborhood of Musca to be aligned with the projected small axis of the filament, and that the polarization pattern, in degree and position angle, is altered across more extinct regions, particularly in the northern region close to the IRAS 12322-7023 source.

Additional insights of Musca can be seen in large-scale structure maps in a molecular survey with low space resolution, of ^{13}CO ($J = 1$–0) and ^{12}CO ($J = 1$–0), carried out by Mizuno et al. (1998) and Mizuno et al. (2001), respectively, in the Chamaeleon–Musca complex. Recently, Hacar et al. (2016) studied the kinematics properties of Musca through ^{13}CO and $C^{18}O$ ($J = 2$–1) lines and concluded that Musca is entirely subsonic and velocity coherent and that its internal gas kinematics is dominated by thermal motions.

On the other hand, Kainulainen et al. (2016) analyzed the overall fragmentation process in Musca, concluding that the

fragmentation started a few tenths of a megayear ago from the ends of the cloud. They also studied the stability of the center region of Musca and concluded that it is in good agreement with the predictions of the pressure-confined hydrostatic equilibrium model. Earlier, Vilas-Boas et al. (1994), analyzing the line mass density of Musca, stated that the entire filament seems to be self-gravitating.

Observation and characterization of the condensations embedded in Musca had been done from CO line emissions (Vilas-Boas et al. 1994; Löhr et al. 2007), dust emission (Juvela et al. 2010, 2011, 2012), and dust extinction (Kainulainen et al. 2016), but none of these studies had analyzed the stability of the cores embedded in those condensations. However, determining whether a core is gravitationally bound or unbound is important for understanding whether it will form a star.

In this work we study the stability of dense cores embedded in Musca, which have extinction peaks greater than 10 mag and are potential sites of star formation (Johnstone et al. 2004; Lada et al. 2010; Kainulainen et al. 2011), through the Bonnor–Ebert isothermal sphere model. We derive their fundamental physical parameters such as size, temperature, mass, and external pressure and explore their physical properties using $J = 1$–0 transitions of ^{13}CO and C^{18}O. For the first time, we report the observation of the $J = K = 1$ transition of NH_3 toward Mu13.

The paper is organized as follows. In Section 2 we described briefly the observations, the data reduction, and analysis processes. In Section 3 we present the results, which are discussed in Section 4. Finally, in Section 5 we summarize the results.

2. Methodology: Observations, Data Reduction, and Analysis

2.1. 2MASS Data

To construct the extinction maps, we used the Near Infrared Color Excess (NICE) method and the NIR data extracted from the Two Micron All Sky Survey (2MASS) Point Source Catalog (PSC).

2MASS (Skrutskie et al. 2006) is a whole-sky survey in three infrared wavebands around 2 μm, done with two telescopes of 1.3 m diameter, located in Mount Hopkins (Arizona, USA) and Cerro Tololo (Chile). Each point on the sky was observed during 7.8 s, with a 10σ point-source detection level. The 2MASS PSC contains 471 millions stars, covering 99.99% of the sky[6] in J (1.24 μm), H (1.66 μm), and K_s (2.16 μm) bands, with threshold magnitudes of 15.8, 15.1, and 14.3, respectively.

2.2. The NICE Method

The NICE method combines direct measurements of NIR color excess and uses a control field region, supposedly free of reddening, as a reference, to measure the extinction in the studied cloud (on-cloud), assuming that the stellar population is similar in both regions (Lada et al. 1994).

If the intrinsic color of a star is known, its color excess $E(H - K)$ is given by

$$E(H - K) = (H - K)_{\rm obs} - (H - K)_{\rm intr}, \quad (1)$$

where $(H - K)_{\rm obs}$ is the $H - K$ observed color for each star in the on-cloud region and $(H - K)_{\rm intr}$ is the intrinsic color, approximated by the average color of the control field stars, $(H - K)_{\rm intr} = \overline{(H - K)_{\rm cont}}$.

From the 2MASS PSC we retrieved the HK magnitudes of the on-cloud and of the control field stars and their corresponding uncertainties $\sigma_{H,K}$. We used stars with $H \leqslant 15.5$ mag, $K \leqslant 15.0$ mag, and $\sigma_{H,K} \leqslant 0.1$ mag, ensuring that the signal-to-noise ratio (S/N) is greater than 10. We removed foreground stars with color excess $E(H - K) < \sigma_{H-K}$ to avoid contamination in the extinction estimates. The stars of the control field region, with equatorial coordinates R.A$_{\rm J2000.0} = 12^{\rm h}09^{\rm m}50^{\rm s}$ and decl.$_{\rm J2000.0} = -71°03'30''$, have intrinsic colors $(H - K) = 0.145 \pm 0.08$ mag.

The estimated color excess was converted to visual extinction ($A_{\rm V}$) using the reddening law in the 2MASS system given by (Nielbock & Chini 2005)

$$A_{\rm V} = 19.4E(H - K), \quad (2)$$

and the associated visual extinction uncertainty is given by (Racca et al. 2009)

$$\sigma_{A_{\rm V}} = 19.4\sqrt{\sigma_i^2 + \sigma_{\rm cont}^2}, \quad (3)$$

where σ_i is the uncertainty in the observed $H - K$ color excess and $\sigma_{\rm cont}$ is the standard deviation of colors in the control field.

The spatial distribution of stars toward the cloud is nonuniform. In order to have a uniformly sampled extinction map, the data were smoothed by spatially convolving the extinction measurements with a Gaussian filter (kernel) with a given smoothing parameter (h) and finally sampled the map at the Nyquist frequency (Lada et al. 1994). The Gaussian filter is given by

$$K(\alpha, \alpha_i, \delta, \delta_i) = \frac{1}{2}\exp\left(-\frac{r_i^2}{2h^2}\right), \quad (4)$$

where $r_i^2 = (\delta - \delta_i)^2 + (\alpha - \alpha_i)^2\cos^2(\delta)$.

The choice of the smoothing parameter is a compromise between a final map with high S/N and good resolution. We used $h = 40''$ for the entire extinction map of Musca. In this map, we identified condensations that have cores with visual extinction greater than 10 mag and constructed their visual extinction maps using $h = 30''$. We tested other values. When h is greater than the chosen values, the maps lose details, and when they are smaller, the maps are very noisy. The chosen resolutions ensure an S/N greater than 3.

The visual extinction at each point in the map is calculated by

$$A_{\rm V}(\alpha, \delta) = \frac{\sum_{i=1}^{n} K(\alpha, \alpha_i, \delta, \delta_i) \times A_{\rm V}(\alpha_i, \delta_i)}{\sum_{i=1}^{n} K(\alpha, \alpha_i, \delta, \delta_i)}, \quad (5)$$

where n is the total number of stars in the on-cloud region. The $A_{\rm V}(\alpha_i, \delta_i)$ is given by Equation (2), and the associated uncertainty is given by Equation (8) of Racca et al. (2009).

2.3. Internal Structure of Cores with High Extinction Peaks

To study the cores with $A_{\rm V} > 10$ mag, we identified the location of the peak extinction in each condensation, setting it as the central position to construct the averaged radial extinction profile as described in Racca et al. (2009). In our case, we set concentric annuli at each core center, 30″ wide,

[6] Hereafter, filter "K_s" will be called "K."

and averaged the extinction at the Nyquist frequency, obtaining a mean extinction value at every 15″. Then, the obtained visual extinction profiles were fitted with a Bonnor–Ebert isothermal sphere.

A Bonnor–Ebert (Ebert 1955; Bonnor 1956) sphere is a self-gravitating sphere of gas in hydrostatic equilibrium. The pressure and density at each point in the Bonnor–Ebert sphere are described by the modified equation of Lane–Emden:

$$\frac{1}{\xi^2}\frac{d}{d\xi}\left(\xi^2\frac{d\phi}{d\xi}\right) = e^{-\phi}, \quad (6)$$

where $\phi(\xi) = -\ln(\rho/\rho_c)$, $\xi = (r/a)\sqrt{4\pi G\rho_c}$ is the dimensionless radius, ρ_c is the finite central density, ρ is the density at each point and is given by $\rho = \rho_c e^{-\phi(\xi)}$, a is the isothermal sound speed ($a^2 = P/\rho = k_B T/\mu m_H$), and G is the gravitational constant.

Ebert (1955) and Bonnor (1956) demonstrated that the value of ξ, at the external radius of the sphere R, provides a stability measure. The stability parameter (ξ_{max}) is estimated by

$$\xi_{max} = \frac{R}{a}\sqrt{4\pi G\rho_c}. \quad (7)$$

The critical state has $\xi_{max} = 6.5$, which corresponds to a center-to-edge density contrast equal to 14 and describes spheres marginally bounded. Systems with $\xi_{max} > 6.5$ are unstable to gravitational collapse and have center-to-edge density contrast greater than 14. Systems with $\xi_{max} < 6.5$ are stable and have center-to-edge density contrast less than 14.

In order to compare Bonnor–Ebert theoretical profiles with the observed profiles for each core, we solved numerically Equation (6) and constructed a series of theoretical Bonnor–Ebert profiles for various values of the stability parameter ξ_{max} and temperature T. Then we obtained the volumetric density $n(r)$ and integrated it along the line of sight to obtain the hydrogen column density profile.

To express the column density in terms of visual extinction, we used the gas-to-dust ratio given by (Bohlin et al. 1978; Savage & Mathis 1979)

$$N_{H_2} = 0.94 \times 10^{21} A_V \text{ cm}^{-2} \text{ mag}^{-1}, \quad (8)$$

since we are considering regions with $A_V \geqslant 3$ mag, where almost all hydrogen is in its molecular form (Hollenbach et al. 1971; Whittet et al. 1987; van Dishoeck & Black 1988; Caselli & Ceccarelli 2012).

The stability parameter was varied from 3 to 15 in steps of $\Delta\xi = 0.1$, and the temperature was varied from 5 to 30 K in steps of $\Delta T = 0.1$ K. The uncertainty of each fit and of the best-fit parameters was estimated by Equations (25) and (26) of Racca et al. (2009), respectively. The best-fit Bonnor–Ebert parameters (ξ_{max} and T) were that with a minimum value of χ_r^2. Knowing the stability parameter and the radius of the core, which is defined as the distance from the center of the core where the Bonnor–Ebert fit reaches a *plateau* level of extinction, we estimated the physical parameters of the cores using the approach given by Racca et al. (2009).

2.4. Observations of ^{13}CO and $C^{18}O$

The observations of the $J = 1$–0 transition of ^{13}CO at 110.2 GHz and the $J = 1$–0 transition of $C^{18}O$ at 109.8 GHz were made in 1992 October, with the 15 m Swedish-ESO Submillimeter Telescope (SEST) at La Silla, Chile. The receiver front-end was based on a Schottky diode waveguide mixer followed by an intermediate-frequency amplifier. The system temperature was typically 370–420 K. The acousto-optical spectrometer had 2048 channels, with a spectral resolution of 0.12 km s^{-1} and a total bandwidth of 100 MHz. The spectra were obtained using an overlap frequency switching mode with 7 MHz frequency shift and integrated during 2 minutes for ^{13}CO and 6 minutes for $C^{18}O$. The observations were calibrated against a cold load to obtain the correction for atmospheric attenuation. The half-power beam width was 48″, and the beam efficiency was 0.9. The rms pointing accuracy was greater than 10″, and it was checked systematically by observing SiO masers from VYCMa, Ik Tau, and R Car.

2.5. Observations of NH_3

The observations of the $J = K = 1$ transition of NH_3 at 23.7 GHz were made in 1994 May, with the 64 m Parkes radio telescope, in Australia. The digital correlator had 1024 channels, with spectral resolution of 0.1 km s^{-1} and total bandwidth of 126 km s^{-1}. The FWHM of the main beam was 81″, and the beam efficiency was 0.32. The system temperature was 70 K, and the rms noise in the antenna temperature was typically 0.03 K. The spectra were also taken using an overlap frequency switching mode, with 2.6 MHz frequency shift. The integration time for each observation was 150 s. The B228 was used as a calibrator.

2.6. Line Emission Data Reduction

The ^{13}CO, $C^{18}O$, and NH_3 data were reduced using the line analysis software DRAWSPEC[7] and GILDAS.[8] Each position was observed several times. After the baseline correction of all spectra, the spectra were averaged for each position. The final spectrum was folded and then fitted with a Gaussian function. The derived parameters from Gaussian fitting are given in Table 1 for ^{13}CO and $C^{18}O$. The condensation names are according to Vilas-Boas et al. (1994).

Differently from Vilas-Boas et al. (1994), who observed only the center position of each condensation, we observed many positions in eight condensations; however, in Table 1 we give data of four condensations, whose cores were modeled by Bonnor–Ebert spheres. We presented only data of the center position and one position at the north, south, east, and west of the center position, where we have observations of both ^{13}CO and $C^{18}O$.

In Table 2 we give the fitted parameters of NH_3 lines. The fitted parameters were used to estimate the optical depth at the peak of the line, excitation temperature, column density, and different masses of the gas in each condensation.

2.7. Gas Properties Derived from ^{13}CO and $C^{18}O$ Emissions

The physical properties of the gas were estimated from ^{13}CO and $C^{18}O$ lines assuming that the gas is in local thermodynamic equilibrium (LTE; Dickman 1978b) and using four assumptions: (1) the beam efficiency times filling factor is the same for both ^{13}CO and $C^{18}O$; (2) the ^{13}CO and $C^{18}O$ lines are formed in similar excitation conditions, and the difference of the excitation temperatures is less than the uncertainty in the deduced values due to the noise in the spectrum; (3) the column

[7] http://www.cv.nrao.edu/~hliszt/programs.html
[8] http://www.iram.fr/IRAMFR/GILDAS

Table 1
Observed Parameters of ^{13}CO and C^{18}O in the Densest Condensations of Musca

Cond.	Observed Position			^{13}CO			C^{18}O		
	Pos. Name	R.A.$_{J2000.0}$ (h:m:s)	Decl.$_{J2000.0}$ (°: ′: ″)	T_A^* (K)	V_c (km s^{-1})	ΔV (km s^{-1})	T_A^* (K)	V_c (km s^{-1})	ΔV (km s^{-1})
(1)	(2)	(3)	(4)	(5)	(6)	(7)	(8)	(9)	(10)
Mu4	Mu4-1	12 24 23.00	−71 54 33.2	3.46 ± 0.07	2.87 ± 0.01	0.65 ± 0.02	0.65 ± 0.04	2.88 ± 0.01	0.45 ± 0.03
	Mu4-2	12 23 57.24	−71 52 33.2	3.87 ± 0.06	2.99 ± 0.01	0.72 ± 0.01	0.84 ± 0.04	3.08 ± 0.01	0.57 ± 0.03
	Mu4-3[a]	12 24 23.00	−71 52 33.2	4.17 ± 0.07	2.99 ± 0.01	0.76 ± 0.01	1.16 ± 0.04	3.07 ± 0.01	0.54 ± 0.02
	Mu4-4	12 24 48.67	−71 52 33.2	2.99 ± 0.10	2.95 ± 0.01	0.59 ± 0.02	0.28 ± 0.04	3.10 ± 0.05	0.72 ± 0.12
Mu5	Mu5-1	12 25 24.66	−71 43 15.0	4.17 ± 0.28	3.14 ± 0.04	1.18 ± 0.09	1.15 ± 0.07	3.38 ± 0.02	0.68 ± 0.05
	Mu5-2	12 24 59.15	−71 41 15.0	4.02 ± 0.25	3.06 ± 0.02	0.77 ± 0.05	0.48 ± 0.05	3.13 ± 0.03	0.60 ± 0.07
	Mu5-3[a]	12 25 24.62	−71 41 15.0	4.15 ± 0.30	3.09 ± 0.03	0.92 ± 0.08	1.18 ± 0.08	3.23 ± 0.02	0.62 ± 0.04
	Mu5-4	12 25 50.10	−71 41 15.0	3.70 ± 0.24	3.15 ± 0.03	1.01 ± 0.08	1.12 ± 0.09	3.39 ± 0.02	0.50 ± 0.05
	Mu5-5	12 25 24.58	−71 39 15.0	3.90 ± 0.26	2.93 ± 0.03	0.94 ± 0.07	0.62 ± 0.06	3.12 ± 0.03	0.60 ± 0.07
Mu10	Mu10-1	12 30 55.50	−71 04 52.0	2.35 ± 0.47	2.85 ± 0.06	0.47 ± 0.13	⩽0.06	...	...
				4.22 ± 0.32	3.59 ± 0.05	0.77 ± 0.11	1.27 ± 0.10	3.55 ± 0.02	0.48 ± 0.04
	Mu10-2	12 30 30.82	−71 02 52.0	2.17 ± 0.33	2.98 ± 0.07	0.50 ± 0.14	⩽0.06	...	...
				3.62 ± 0.31	3.60 ± 0.04	0.52 ± 0.09	1.10 ± 0.09	3.65 ± 0.01	0.36 ± 0.03
	Mu10-3[a]	12 30 55.45	−71 02 52.0	3.77 ± 0.22	3.33 ± 0.03	0.98 ± 0.07	1.31 ± 0.10	3.57 ± 0.02	0.59 ± 0.05
	Mu10-4	12 31 20.08	−71 02 52.0	4.19 ± 0.26	3.32 ± 0.03	0.86 ± 0.06	1.16 ± 0.09	3.43 ± 0.02	0.59 ± 0.01
	Mu10-5	12 30 55.41	−71 00 52.0	3.66 ± 0.23	3.35 ± 0.03	0.89 ± 0.66	0.56 ± 0.05	3.44 ± 0.02	0.48 ± 0.05
Mu13	Mu13-1	12 35 06.40	−70 42 47.0	4.21 ± 0.28	3.01 ± 0.03	0.81 ± 0.06	0.62 ± 0.07	3.08 ± 0.04	0.77 ± 0.10
	Mu13-2	12 34 42.17	−70 40 49.0	1.23 ± 0.09	3.19 ± 0.03	0.78 ± 0.07	⩽0.06	...	...
	Mu13-3[a]	12 35 06.35	−70 40 47.0	4.22 ± 0.39	3.09 ± 0.05	0.67 ± 0.10	0.43 ± 0.05	3.16 ± 0.09	0.89 ± 0.21
				2.35 ± 0.33	3.95 ± 0.11	0.79 ± 0.23	0.29 ± 0.08	3.99 ± 0.01	0.53 ± 0.20
	Mu13-4	12 35 30.53	−70 40 45.0	3.44 ± 0.35	2.92 ± 0.05	0.62 ± 0.11	0.39 ± 0.07	2.90 ± 0.06	0.60 ± 0.13
				2.84 ± 0.30	3.74 ± 0.07	0.75 ± 0.16	0.62 ± 0.08	3.82 ± 0.03	0.49 ± 0.08
	Mu13-5	12 35 06.30	−70 38 47.0	3.79 ± 0.26	3.10 ± 0.03	0.66 ± 0.07	0.42 ± 0.06	3.10 ± 0.04	0.58 ± 0.10
				1.09 ± 0.27	3.95 ± 0.09	0.55 ± 0.21	⩽0.06	...	...

Notes. Column (1) gives the condensation name, and column (2) gives the observed position. The equatorial coordinates of each position are given in columns (3) and (4). Columns (5)–(7) give the antenna temperature corrected for atmospheric attenuation (T_A^*), the radial velocity in the center line (V_c), and the observed line width (ΔV) of ^{13}CO, respectively. Columns (8)–(10) give the same parameters for C^{18}O. The estimated uncertainties for all parameters were obtained from the fitted Gaussians.
[a] Central position of each condensation.

Table 2
Observed Parameters of NH_3 toward Mu13

Cond.	Pos. Name	R.A.$_{J2000.0}$ (h:m:s)	Decl.$_{J2000.0}$ (°: ′: ″)	T_A^* (K)	V_c (km s^{-1})	ΔV_{obs} (km s^{-1})
Mu13	Mu13-6	12 35 18.18	−70 39 46.8	0.24 ± 0.01	3.90 ± 0.02	0.77 ± 0.05
				0.07 ± 0.01	−3.79 ± 0.01	1.08 ± 0.03
				0.08 ± 0.02	11.48 ± 0.03	0.46 ± 0.08

Note. The NH_3 spectra were Hanning smoothed and decimated to a velocity resolution of 0.3 km s^{-1}.

density ratio of ^{13}CO and C^{18}O is ∼5.5, which is the terrestrial abundance ratio; and (4) in each condensation, the observed ^{13}CO and C^{18}O lines are formed in the regions with the same velocity gradient (Myers et al. 1983).

The optical depth of the C^{18}O line, τ_{18}, was calculated using the ratio of the observed antenna temperatures of ^{13}CO and C^{18}O, given by

$$\frac{T_{A13}^*}{T_{A18}^*} = \frac{1 - \exp(-5.5\tau_{18})}{1 - \exp(-\tau_{18})}, \quad (9)$$

where T_A^* is the observed antenna temperature corrected for atmospheric opacity. The subscripts 13 and 18 correspond to ^{13}CO and C^{18}O, respectively.

The excitation temperature of C^{18}O line was calculated by

$$\frac{T_0}{T_{18}} = \ln\left[1 + \frac{T_0}{J(T_{\rm CMB}) + T_{A18}^*/[\eta_b\eta_f(1 - e^{-\tau_{18}})]}\right], \quad (10)$$

where $T_0 = h\nu_0/k_{\rm B}$, ν_0 is the transition frequency for C^{18}O, $k_{\rm B}$ and h are the Boltzmann and Planck constants, respectively, $T_{\rm CMB} = 2.7$ K is the temperature of background radiation, $J(T) = T_0/[\exp(T_0/T) - 1]$ is the Planck distribution function with temperature T, η_b is the beam efficiency, and η_f is the filling factor, which is assumed to be 1.

Assuming that the absorption is constant through the cloud, the column density in the $J = 1$ rotational level is given by

(Myers et al. 1983)

$$N_{18}(J=1) = 3.6 \times 10^{14} \tau_{18} J(T_{18}) \Delta V_{18} \text{ cm}^{-2}, \quad (11)$$

where ΔV is the line width in km s^{-1}, which is obtained by removing the spectrometer resolution ($\Delta V_{\rm res}$) from the observed line width and is given by

$$\Delta V = \sqrt{\Delta V_{\rm obs}^2 - \Delta V_{\rm res}^2}. \quad (12)$$

The thermal line broadening was determined by

$$\Delta V_{\rm th}^2 = 8 \ln 2 \frac{k_{\rm B} T_k}{m_0}, \quad (13)$$

where m_0 is the mass of the observed molecule and $T_k \equiv T_{\rm exc} = T_{18}$.

The contribution of nonthermal motions is calculated, discounting the thermal broadening from the line width, by

$$\Delta V_{NT}^2 = \Delta V^2 - \Delta V_{\rm th}^2. \quad (14)$$

The total $C^{18}O$ column density is obtained by multiplying $N_{18}(J=1)$ by the classical partition function ratio, which is given by

$$f^{-1} = \frac{\sum_{J=0}^{J_{\rm max}} (2J+1) \exp[-hBJ(J+1)/k_{\rm B} T_{18}]}{3 \exp(-2hB/k_{\rm B} T_{18})}, \quad (15)$$

where $B = 54.89$ GHz is the $C^{18}O$ rotation constant. The sum was truncated at $J_{\rm max} = 5$, where the change in the sum is less than 0.1%.

To estimate the visual extinction, we used the empiric equation from Vilas-Boas et al. (1994), derived from a linear fit to ^{13}CO and $C^{18}O$ observation data:

$$A_{\rm V}^{\rm CO} = 1.8 \times 10^{-15} N(C^{18}O) + 2.2 \text{ mag}. \quad (16)$$

The condensations are assumed as uniform spheres of gas and dust with average volumetric density given by

$$\overline{n(H_2)} = \frac{N(H_2)}{L}, \quad (17)$$

where the column density of molecular hydrogen was derived using the gas-to-dust ratio given by Equation (8) and L is the optical size of each condensation.

The corresponding LTE mass of the condensations was estimated by

$$M_{H_2} = 22.2 \left[\frac{N(H_2)}{10^{21} \text{ cm}^{-2}} \right] \left(\frac{L}{\text{pc}} \right)^2 M_\odot, \quad (18)$$

and the Jeans mass was calculated using (Evans 1999)

$$M_{\rm J} = \frac{18 T_k^{3/2}}{n^{1/2}} M_\odot, \quad (19)$$

where the total particle density is $n = n(H_2) + n(He) \approx 2.3 \overline{n(H_2)}$.

Based on assumptions (1)–(4) stated earlier, we find the same parameters for ^{13}CO. We also estimated the virial mass from ^{13}CO line widths by (Evans 1999)

$$M_{\rm V} = C_v G^{-1} r (\Delta V_{13})^2 = 210 \, C_v \, r(\text{pc}) [\Delta V_{13}(\text{km s}^{-1})]^2 \, M_\odot, \quad (20)$$

where $r = L/2$ and C_v is a constant that depends on the cloud structure. Usually it is assumed to be 1 (McKee & Zweibel 1992).

2.8. Gas Properties Derived from NH_3 Emission

To estimate the optical depth of the main hyperfine component of the $J = K = 1$ transition of NH_3, it is assumed that the beam filling factor and the excitation temperature for all hyperfine transitions are equal and are in LTE (Ho & Townes 1983). It is calculated from the ratio of the hyperfine brightness temperatures of the main and satellite components by (Barrett et al. 1977)

$$\frac{T_{\rm B}(1,1,m)}{T_{\rm B}(1,1,s)} = \frac{1 - e^{-\tau(1,1,m)}}{1 - e^{-a\tau(1,1,m)}}, \quad (21)$$

where a is the relative intensity of the satellite to the main hyperfine component, and $T_{\rm B}(1,1,m)$ and $T_{\rm B}(1,1,s)$ are the brightness temperature of the main and satellite hyperfine components, respectively.

The excitation temperature of the $J = K = 1$ transition of NH_3 is derived by (Gardner et al. 1985)

$$T_A^* = \eta_b [J(T_{\rm exc}) - J(2.7)][1 - \exp(-\tau_{1,1,m})], \quad (22)$$

where T_A^* is the antenna temperature corrected for atmospheric attenuation and $J(2.7)$ is the Planck function for the cosmic background radiation.

To estimate the kinetic temperature, we used the relation (Walmsley & Ungerechts 1983)

$$T_{\rm rot} = \frac{T_k}{1 + (T_k/41) \ln[1 + 1.5 \exp(-16/T_k)]}. \quad (23)$$

For populations in LTE, the rotational temperature is equal to the excitation temperature ($T_{\rm rot} = T_{\rm exc}(2,2;1,1) \equiv T_{\rm exc}(1,1)$; Mangum et al. 1992).

To derive the column density for the $J = K = 1$ transition of the NH_3 line, we used the equation (Mangum et al. 1992)

$$N(1,1) = 6.6 \times 10^{14} \frac{T_{\rm exc}}{\nu(1,1)} \tau(1,1,m) \Delta V \text{ cm}^{-2}, \quad (24)$$

where $\nu(1,1)$ is the transition frequency in GHz and ΔV is the line width in km s^{-1}, derived from Equation (12).

The total column density of NH_3 is estimated by (Lu et al. 2014)

$$N(NH_3) \approx 0.0138 \times N(1,1) \exp\left(\frac{23.1}{T_{\rm rot}} \right) T_{\rm rot}^{3/2}. \quad (25)$$

3. Results

3.1. Properties of Dense Cores Embedded in Musca

In Figure 1 we show the 40″ resolution visual extinction map of Musca delimited by a contour level of 3 mag. In this map we can resolve several condensations, and we label the five densest, whose embedded cores have extinction peaks greater than 10 mag.

The 30″ resolution visual extinction map of the labeled condensations and the radial extinction profile of the embedded cores are shown in Figure 2 and in Figures 4–7 below. Mu1 was not fitted by a Bonnor–Ebert isothermal sphere, due to its radial profile, which does not meet our adherence test.

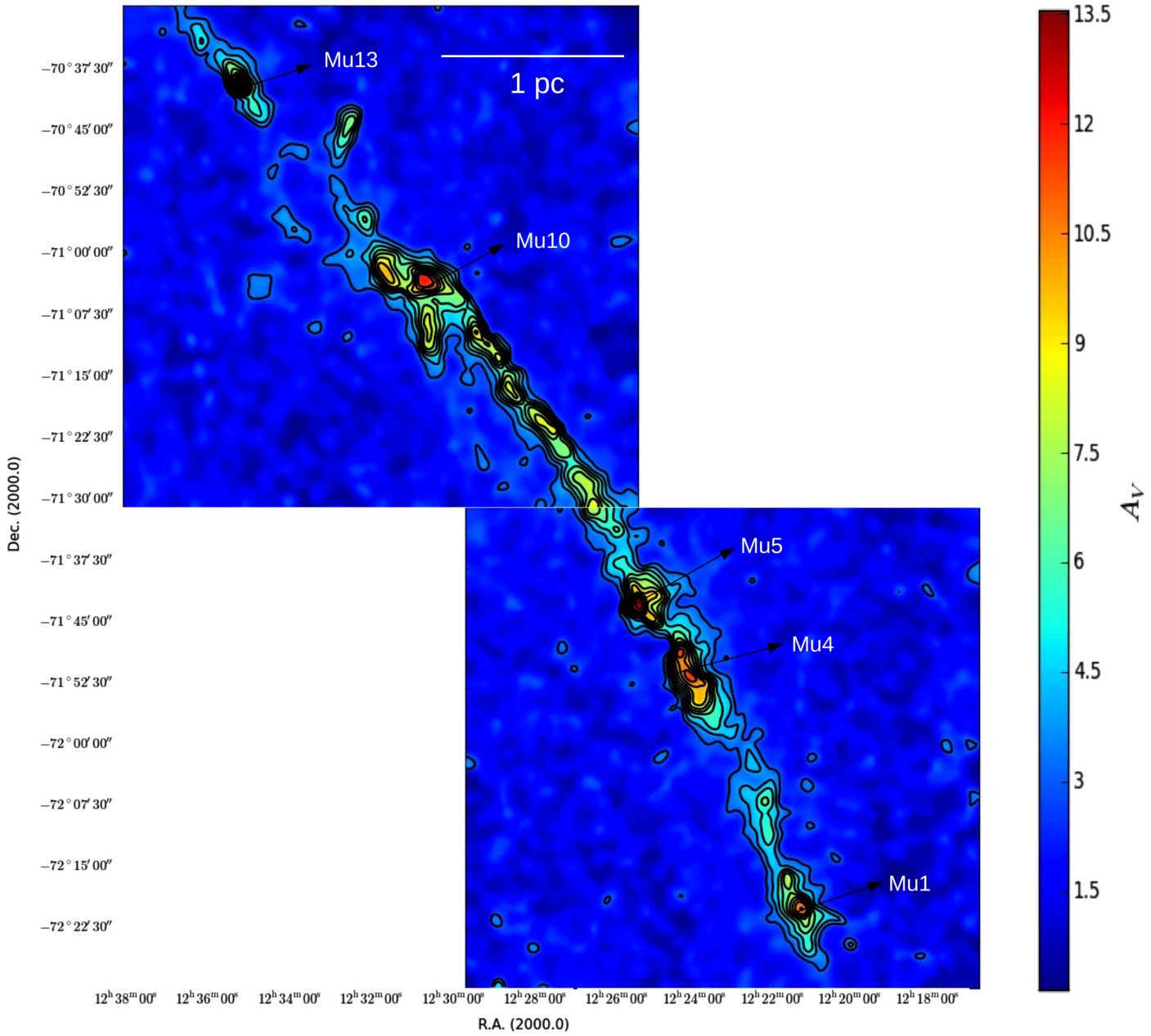

Figure 1. Musca visual extinction map with 40″ resolution. The extinction contour levels start at 3 mag and increase in steps of 1 mag. The maximum value is 13.6 mag. Labeled are condensations whose embedded cores have extinction peaks greater than 10 mag and at least two subsequent extinction contours spaced by intervals of 1 mag, whose properties are discussed in the text.

In the extinction maps, the extinction is codified in a color scale, where blue represents the minimum and red represents the maximum value reached in each region. The bar at the right side gives the extinction value in mag. The solid lines showing the levels of constant extinction are superimposed to the maps. In the radial extinction profiles, the solid line represents the best-fitted Bonnor–Ebert theoretical profile, and in the box are given the best-fit stability parameter and the Bonnor–Ebert temperature.

In Table 3 are summarized the physical parameters of the embedded cores derived from Bonnor–Ebert sphere model fits. Column (1) gives the core name, column (2) the stability parameter, column (3) the Bonnor–Ebert temperature, column (4) the central volumetric density, column (5) the Bonnor–Ebert mass, column (6) the external pressure, and column (7) the central extinction peak after removing the *plateau* level, which is given in column (8). Column (9) gives the radius of each core, and finally, column (10) gives the value of χ^2_r.

The gas physical parameters of the condensations derived from ^{13}CO and C^{18}O lines are given in Table 4, and those derived from NH_3 lines toward Mu13 are given in Table 5. Column (1) of this table gives the observed position, and column (2) the optical depth of the main hyperfine component of transition $J = K = 1$ of NH_3. Columns (3) and (4) give the excitation and kinetic temperatures, respectively. Column (5) gives the column density of NH_3, and column (6) the column density of molecular hydrogen, estimated considering the ratio of H_2 to NH_3 to be $\sim 3 \times 10^{-8}$ (Harju et al. 1993; Urquhart et al. 2015). Column (7) gives the volumetric density, calculated assuming that the Mu13 core has a spherical shape

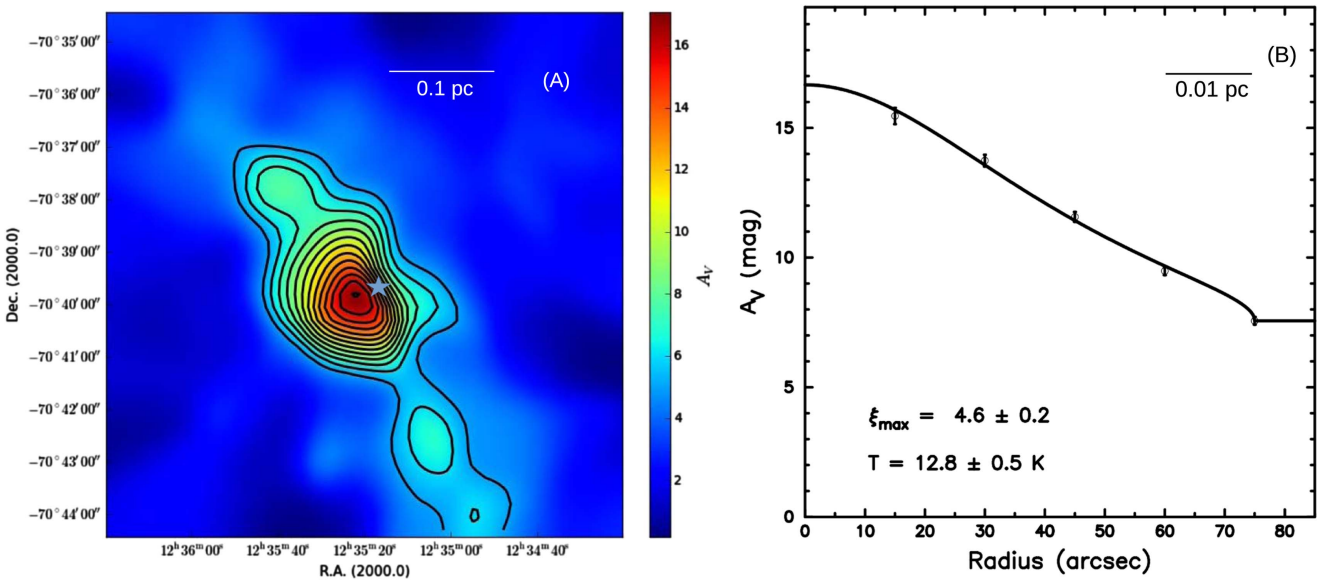

Figure 2. (a) 30″ visual extinction map of Mu13. The contours range from 5 to 17 mag in steps of 1 mag. The star shows the position of IRAS 12322-7023. (b) Visual extinction radial profile of the embedded core. The solid line represents the best-fitted Bonnor–Ebert theoretical profile, and the best-fit stability parameter and the Bonnor–Ebert temperature are given.

Table 3
Properties of the Cores Derived from Bonnor–Ebert Fitting

Core Name	ξ_{max}	T_{BE} (K)	n_c (10^4 cm^{-3})	M_{BE} ($M_\odot$)	P_{ext}/k_B (10^4 cm^{-3} K)	A_V^c (mag)	$A_V^{plateau}$ (mag)	R (pc)	χ_r^2
Mu13	4.6 ± 0.2	12.8 ± 0.5	9.9	1.2	19.9	9.1	7.6	0.05	1.06
Mu10	5.7 ± 0.1	7.1 ± 0.5	4.3	1.0	3.0	4.7	8.1	0.08	0.73
Mu5	5.7 ± 0.1	8.0 ± 0.5	4.9	1.2	3.8	5.3	9.0	0.08	0.48
Mu4A	5.2 ± 0.1	8.4 ± 0.5	5.8	1.0	5.8	5.8	7.2	0.07	0.83
Mu4B	4.5 ± 0.4	7.8 ± 0.6	3.0	1.0	3.8	3.9	8.7	0.08	0.96

with ∼0.05 pc, obtained from the visual extinction radial profile.

3.1.1. Mu13

Figure 2 shows the 30″ resolution extinction map of Mu13 and the radial extinction profile of its core. It harbors the IRAS 12322-7023 source, whose position is indicated by the star in the extinction map. The Mu13 core has a well-defined boundary, and the denser region is almost circular with 0.05 pc, having maximum visual extinction of 17 mag and a *plateau* level of ∼8 mag.

In the observed positions, the antenna temperature of ^{13}CO ranges from 1.1 to 4.2 K, and for C^{18}O it ranges from 0.3 to 0.6 K. The average line width of ^{13}CO is 0.70 ± 0.09 km s^{-1}, and that of C^{18}O is 0.64 ± 0.14 km s^{-1}. The radial velocities of the lines change between 2.9 and 4.0 km s^{-1}, with an observed total velocity dispersion of about 0.4 km s^{-1}.

Several positions in Mu13 show line profiles of both ^{13}CO and C^{18}O with double peaks, shifted by ∼0.8 ± 0.1 km s^{-1}. The same feature was also observed by Vilas-Boas et al. (1994) in the center position of the condensation. Recently, Hacar et al. (2016) detected double peaks only in the $J = 2$–1 transition of ^{13}CO, shifted by ∼1 km s^{-1}, toward the position that coincides with the YSO. Also, one position toward Mu13 shows double peaks of the $J = 1$–0 transition of ^{12}CO (Arnal et al. 1993). According to Vilas-Boas et al. (1994), these lines may be due to expansion, contraction, or superposition of different clouds with different radial velocities, and Hacar et al. (2016) suggest that those lines may be due to the interaction of the embedded object with its envelope.

Due to the occurrence of the *IRAS* source associated with this condensation, we observed 6 × 6 positions in ^{13}CO ($J = 1$–0) and 6 × 4 positions in C^{18}O ($J = 1$–0), spaced by 1′, with 48″ spatial resolution and 0.1 km s^{-1} spectral resolution. Figures 3 (a)–(d) show the intensities of ^{13}CO and C^{18}O emissions, integrated in velocity and centered in the radial velocities, $V_1 = 3.1 \pm 0.1$ km s^{-1} and $V_2 = 3.9 \pm 0.1$ km s^{-1}.

The integrated intensity maps of ^{13}CO and C^{18}O at 3.1 ± 0.1 km s^{-1} (Figures 3(a)–(c)) show structures that are not well correlated. The ^{13}CO map shows two dense structures at the edges and one at the middle. There is weak evidence that the structure seen in ^{13}CO in the southwest may have a counterpart in the distribution of C^{18}O. Maps with better space coverage and higher space resolution are needed to explore whether these structures are correlated or not.

On the other side, the maps of the integrated intensity of both lines in 3.9 ± 0.1 km s^{-1} (Figures 3(b) and (d)) show a similar pattern and only one structure. This structure has an intensity distribution that most closely traces the column density of dust seen in Figure 2. The integrated intensity maps of ^{13}CO and C^{18}O in Mu13 suggest that the double-peaked lines are due to the superposition of clouds with different radial velocities seen in the line of sight.

The radial velocity of the $J = K = 1$ transition of NH_3 in Mu13 is 3.9 ± 0.2 km s^{-1}, which is equal to the velocity of

Table 4
Properties of the Condensations Derived from ^{13}CO and $C^{18}O$ Lines

Pos.	^{13}CO								$C^{18}O$				
	τ_{18}	T_{18} (K)	$N(C^{18}O)$ (10^{15} cm^{-2})	A_V (mag)	$N(H_2)$ 10^{21} cm^{-2})	$\overline{n(H_2)}$ (10^3 cm^{-3})	$M(H_2)$ ($M_\odot$)	M_J ($M_\odot$)	M_V ($M_\odot$)	τ_{13}	$N(^{13}CO)$ (10^{15} cm^{-2})	ΔV_T (km s^{-1})	ΔV_{NT} (km s^{-1})
(1)	(2)	(3)	(4)	(5)	(6)	(7)	(8)	(9)	(10)	(11)	(12)	(13)	(14)
Mu4-1	0.02	52	1.00	4.0	3.8	2.9	15	83	8	0.1	8.2	0.29	0.57
Mu4-2	0.08	15	0.66	3.4	3.2	2.5	12	14	14	0.4	4.6	0.15	0.69
Mu4-3	0.20	10	0.76	3.6	3.4	2.6	13	7	12	1.1	6.0	0.13	0.74
Mu4-4[a]	...	...	0.98	4.0	3.7	2.9	15	7	22	...	4.4	0.13	0.56
Mu5-1	0.21	10	1.01	4.0	3.8	2.4	22	8	24	1.2	9.6	0.13	1.16
Mu5-2[a]	...	...	0.79	3.6	3.4	2.2	20	8	19	...	5.6	0.13	0.75
Mu5-3	0.23	10	1.01	4.0	3.8	2.4	22	8	20	1.3	8.4	0.13	0.90
Mu5-4	0.26	9	0.77	3.6	3.4	2.1	19	7	13	1.4	8.6	0.12	1.00
Mu5-5[a]	...	...	1.15	4.3	4.0	2.6	23	7	19	...	10.0	0.13	0.92
Mu10-1	...	...	...	...	...	...	...	...	...	...	...	...	...
	0.26	9	0.72	3.5	3.3	1.6	31	8	15	1.4	6.5	0.12	0.75
Mu10-2	...	...	...	...	...	...	...	...	...	...	...	...	...
	0.27	8	0.45	3.0	2.8	1.4	27	7	8	1.5	3.7	0.11	0.49
Mu10-3	0.35	8	0.99	4.0	3.7	1.9	35	6	22	1.9	9.2	0.11	0.96
Mu10-4	0.21	10	0.88	3.8	3.6	1.8	33	9	23	1.2	7.1	0.13	0.84
Mu10-5[a]	...	...	0.77	3.6	3.4	1.7	32	9	15	...	8.0	0.13	0.87
Mu13-1[a]	...	...	1.21	4.4	4.1	3.7	12	6	22	...	7.0	0.13	0.79
Mu13-2	...	...	...	...	...	...	...	...	...	...	...	...	...
Mu13-3[a]	...	...	1.14	4.3	4.0	3.6	12	6	29	...	4.7	0.13	0.64
	...	...	0.67	3.4	3.2	2.9	9	7	10	...	5.6	0.13	0.77
Mu13-4[a]	...	...	0.76	3.6	3.3	3.0	10	7	13	...	4.4	0.13	0.60
	0.09	12	0.42	3.0	2.8	2.5	8	10	8	0.5	3.6	0.14	0.73
Mu13-5[a]	...	...	0.74	3.5	3.3	3.0	10	7	12	...	4.6	0.13	0.64
	...	...	...	...	...	...	...	...	...	...	...	...	...

Note. Column (1) gives the observed positions. Columns (2)–(4) give the optical depth, excitation temperature, and column density of $C^{18}O$, respectively. Column (5) gives the visual extinction along the line of sight. Columns (6)–(8) give the column density, volumetric density, and mass of molecular hydrogen, respectively. Columns (9) and (10) give the Jeans and virial mass, respectively. Columns (11) and (12) give the optical depth and column density of ^{13}CO, respectively. Columns (13) and (14) give the thermal and nonthermal broadening of ^{13}CO, respectively.
To estimate the volumetric density of the molecular hydrogen, we used the estimated column density and the optical size (L) of the condensations given in column (9) of Table 2 of Vilas-Boas et al. (1994).
[a] The line ratio of ^{13}CO to $C^{18}O$ was greater than the standard value of 5.5, and $\tau_{18} < 0.01$. In these cases we used the standard temperature of 10 K to estimate the physical parameters of the gas.

Table 5
Physical Parameters Derived from NH_3 Lines toward Mu13

Obs. Pos.	$\tau_{1,1,m}$	T_{exc} (K)	T_k (K)	$N(NH_3)$ (10^{13} cm^{-2})	$N(H_2)$ (10^{21} cm^{-2})	$\overline{n(H_2)}$ (10^4 cm^{-3})
Mu13-6	0.01	8.3	12	9.0	3.0	2.0

^{13}CO and $C^{18}O$ that define the core associated with this condensation. The antenna temperatures of the main and satellite NH_3 lines were 0.24 and 0.07 K, respectively. Its ratio (0.27) suggests that the region where these lines are formed is in thermal equilibrium.

3.1.2. Mu10

Figure 4 shows the extinction map of Mu10 and the radial profile of the dense core embedded in Mu10, which has an elongated and irregular shape, with peak extinction of 12.7 mag and a *plateau* level of 8 mag. Its radius is 0.08 pc.

In Mu10, the antenna temperature of ^{13}CO ranges from 2.0 to 4.0 K, and that of $C^{18}O$ in the positions where it was detected is 1.0 K. The averaged line widths of ^{13}CO and $C^{18}O$ are 0.71 ± 0.20 km s^{-1} and 0.50 ± 0.09 km s^{-1}, respectively. The gas is moving with radial velocity between 2.9 and 3.7 km s^{-1}. Its dispersion is 0.26 km s^{-1} for ^{13}CO and 0.08 km s^{-1} for $C^{18}O$.

Some positions of Mu10 have line profiles of ^{13}CO with double peaks, shifted by $\sim$0.7 km s^{-1}. In the same positions, the line profiles of $C^{18}O$ have a single peak. The same feature was observed by Hacar et al. (2016) in the $J = 2$–1 transition of ^{13}CO and $C^{18}O$.

3.1.3. Mu5

The visual extinction map of Mu5 and its radial extinction profile are shown in Figure 5. The maximum extinction is 14.2 mag, and the profile drops until it reaches a constant level of 9 mag. Its core has a regular and almost round shape, with a radius of 0.08 pc, and shows three tail-like structures, with extinction of 10 mag.

The observed ^{13}CO lines in Mu5 have an almost constant antenna temperature, of approximately 4.0 K. The antenna temperature of the $C^{18}O$ lines was between 0.5 and 1.2 K. The averaged line widths are 0.96 ± 0.13 km s^{-1} and 0.60 ± 0.06 km s^{-1} for ^{13}CO and $C^{18}O$, respectively. The gas is moving with radial velocity between 2.9 and 3.4 km s^{-1}. The

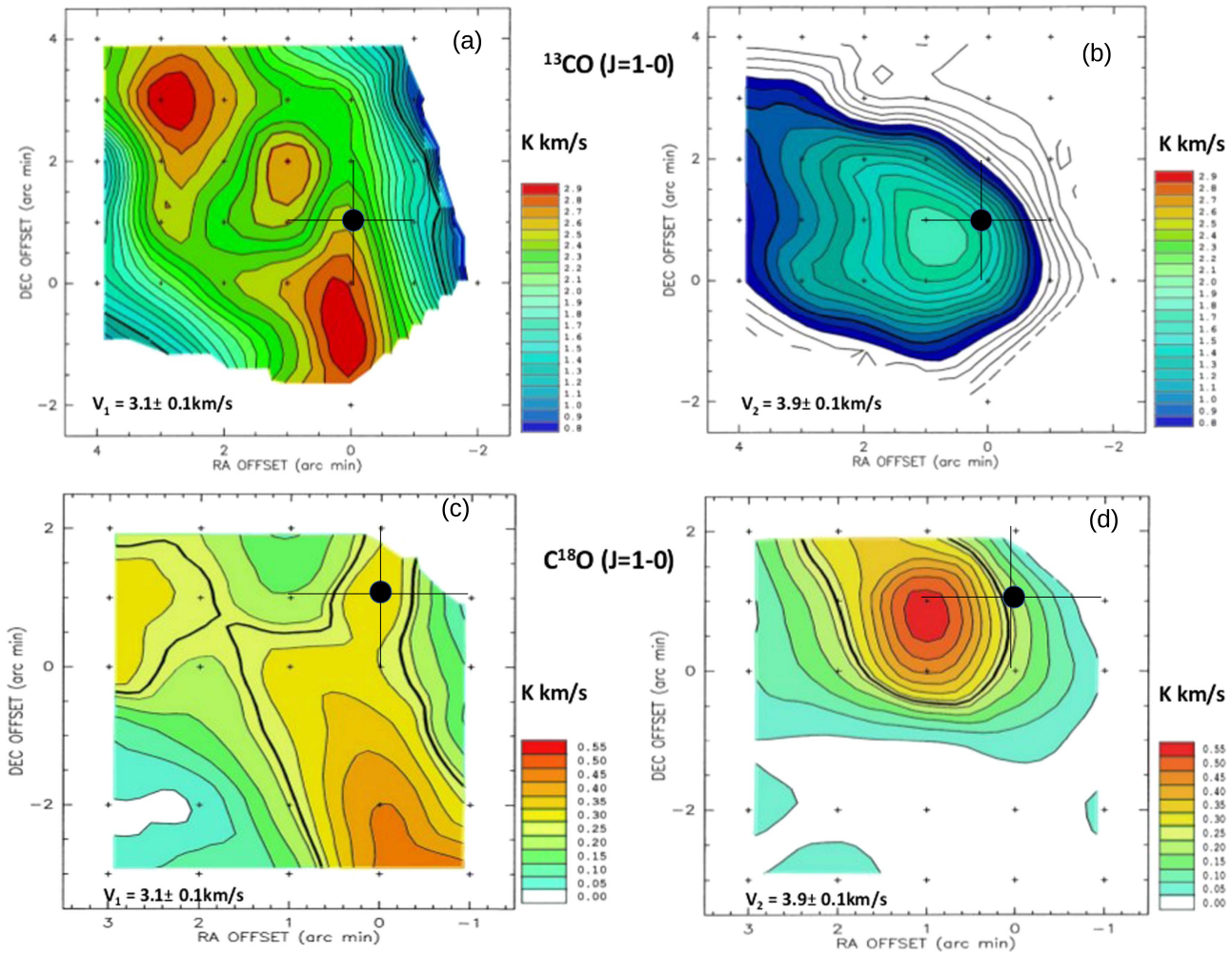

Figure 3. Integrated intensity distribution maps of the $J = 1$–0 transition of ^{13}CO and C^{18}O in Mu13 in $V_1 \sim 3.1 \pm 0.1$ km s^{-1} and $V_2 \sim 3.9 \pm 0.1$ km s^{-1}. The observed positions are marked by plus signs, the filled circles mark the position of the YSO, and the lines represent the position uncertainty. Equatorial coordinates for (0, 0) position are R.A.$_{J2000.0} = 12^h35^m06^s$ and decl.$_{J2000.0} = -70°\ 40'47''$. Panels (a) and (b) show the integrated intensity distribution of ^{13}CO in V_1 and V_2, respectively. The contours start at 0.80 K km s^{-1} and increase in steps of 0.10 K km s^{-1}. Panels (c) and (d) show the integrated intensity distribution of C^{18}O in V_1 and V_2, respectively. The contours start at 0.05 K km s^{-1} and increase in steps of 0.05 K km s^{-1}. The thicker contour corresponds to half of maximum intensity.

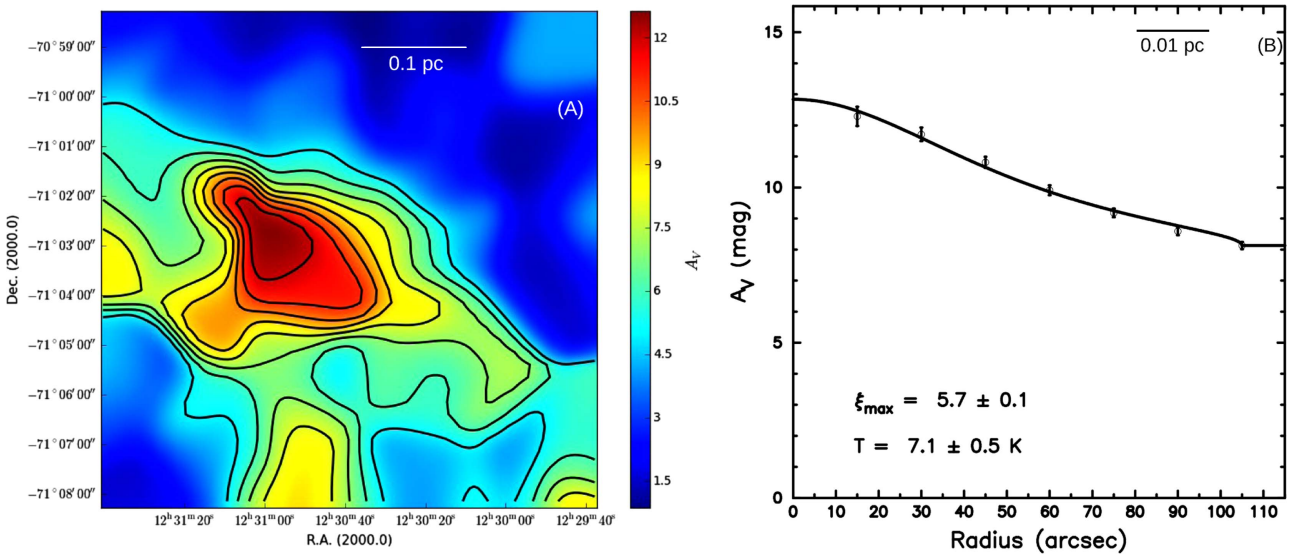

Figure 4. (a) 30″ resolution visual extinction map of Mu10. The extinction contour levels range from 5 mag to 12 mag in steps of 1 mag. (b) Radial extinction profile of the core embedded in Mu10. The solid line represents the best Bonnor–Ebert theoretical profile fitting. The best-fit stability parameter and the Bonnor–Ebert temperature are given.

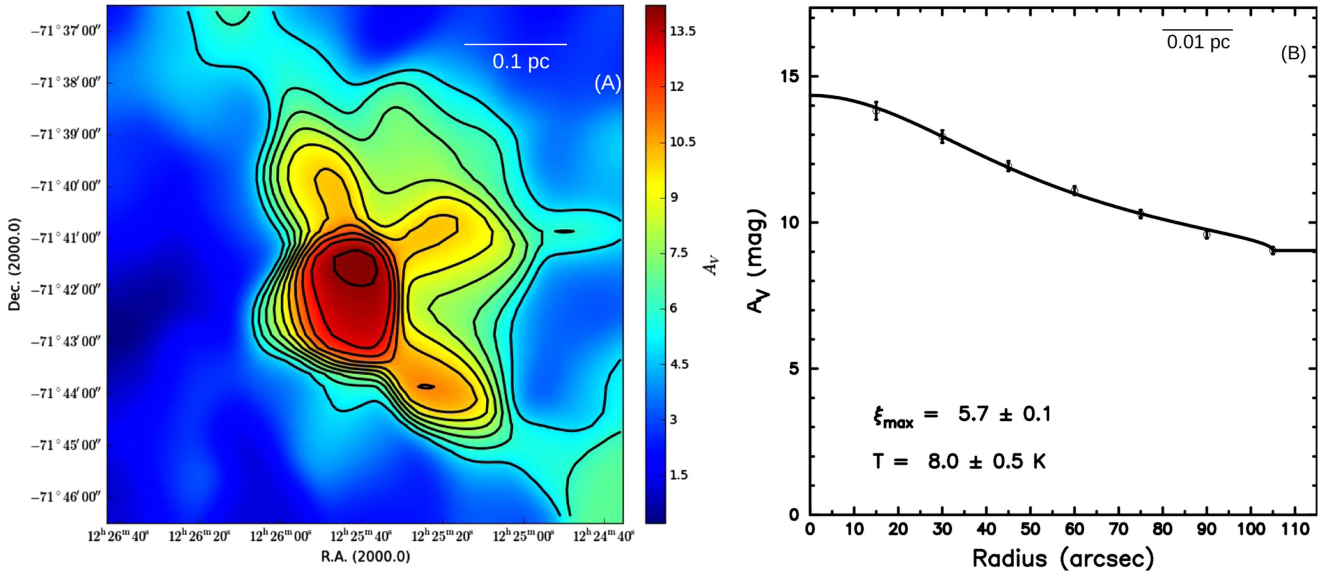

Figure 5. (a) Visual extinction map of Mu5. The extinction contours range from 5 to 14 mag in steps of 1 mag. (b) Extinction radial profile of the embedded core. The solid line represents the best-fit Bonnor–Ebert sphere model, and the best-fit stability parameter and the Bonnor–Ebert temperature are given.

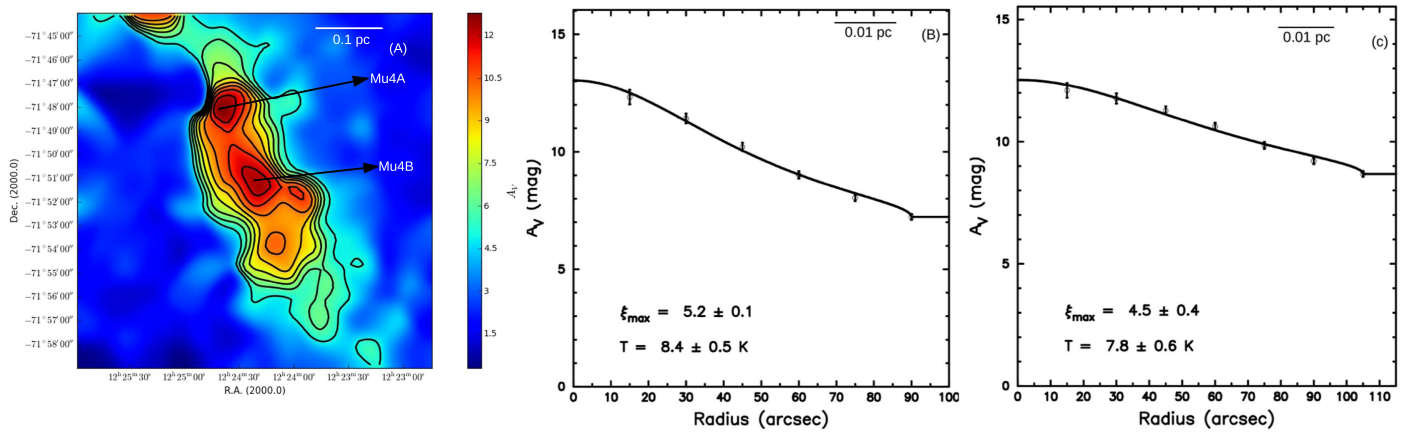

Figure 6. (a) Visual extinction map of condensation Mu4. The extinction contour levels range from 5 to 12 mag in steps of 1 mag. This condensation has two embedded cores, labeled Mu4A and Mu4B, whose radial extinction profiles are in panels (b) and (c), respectively. The solid line represents the best Bonnor–Ebert theoretical profile fitting. The best-fit stability parameter and the Bonnor–Ebert temperature are given.

dispersion of the radial velocity is 0.08 and 0.12 km s^{-1} for ^{13}CO and C^{18}O, respectively.

3.1.4. Mu4

The extinction map of Mu4 is shown in Figure 6. Mu4 is an extended condensation, with two cores embedded, which we labeled as Mu4A and Mu4B, connected by a "bridge" of gas and dust with visual extinction of 10 mag. Mu4A has a round shape, with a radius of 0.07 pc. Its *plateau* is reached at 7 mag. The *plateau* of Mu4B is 9 mag, and its radius is 0.08 pc. The peak extinction of both cores is ∼13 mag. Mu4A is the second-densest core in Musca, with approximately 6×10^4 cm^{-3} derived from the Bonnor–Ebert fit, and it is twice as dense as Mu4B.

In Mu4, the antenna temperature of ^{13}CO was between 3.0 and 4.2 K, and that of C^{18}O ranges from 0.3 to 1.2 K. The averaged line widths are 0.68 ± 0.06 km s^{-1} and 0.57 ± 0.10 km s^{-1} for ^{13}CO and C^{18}O, respectively. The radial velocity of the lines is between 2.9 and 3.1 km s^{-1}, and its dispersion is 0.05 and 0.09 km s^{-1} for ^{13}CO and C^{18}O, respectively.

3.1.5. Mu1

Figure 7 shows the visual extinction map of Mu1 and the extinction radial profile of the embedded core. This core has a round shape, and its extinction peak is approximately 12 mag. Its extinction profile does not fit very well in the Bonnor–Ebert sphere model, due to its flat radial extinction distribution. We do not have observations of ^{13}CO, C^{18}O, or NH_3 in this condensation.

4. Discussion

4.1. The Visual Extinction Map of Musca

The visual extinction map of Musca derived from the 2MASS data and the NICE method traces the boundary of Musca as seen in the visual extinction maps obtained by optical star counts (Gregorio Hetem et al. 1988; Cambrésy 1999) and in large-scale maps of CO emission (Mizuno et al. 1998, 2001).

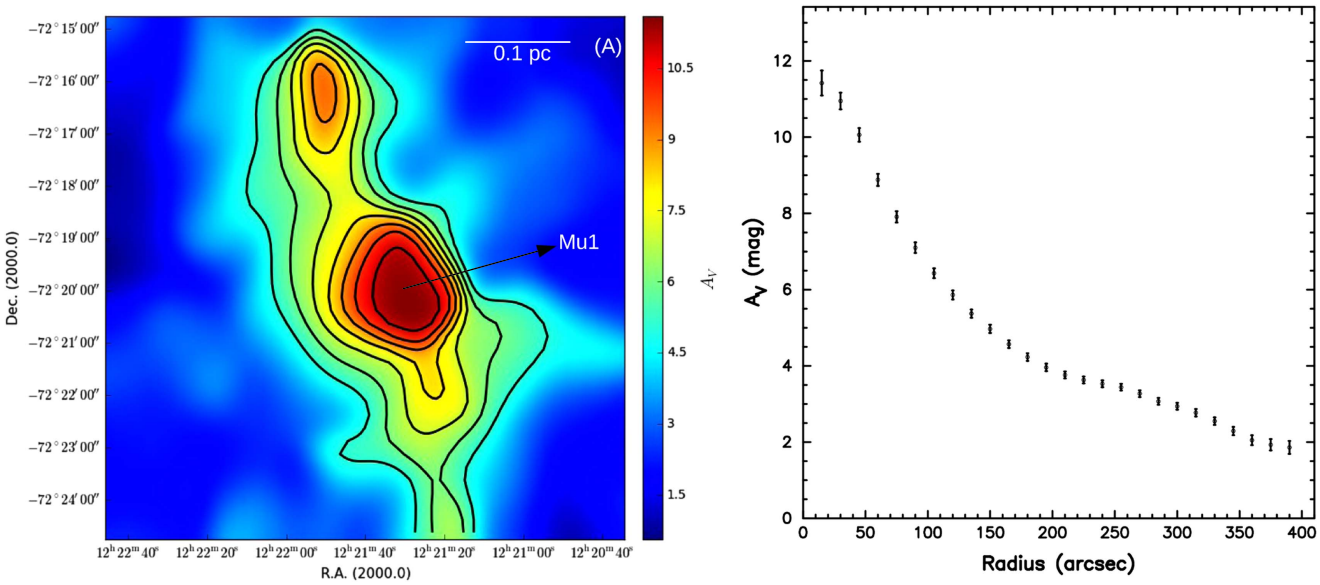

Figure 7. (a) Visual extinction map of Mu1. The extinction contour levels range from 5 to 12 mag in steps of 1 mag. (b) Radial extinction profile of its core. The profile does not fit in the Bonnor–Ebert sphere model.

Also, the map obtained by us shows, in general, a good correlation with that obtained by Kainulainen et al. (2016) using the NICEST method (Lombardi 2009) and data from the NEWFIRM and 2MASS surveys, superimposed with the continuum dust emission at 870 μm and smoothed down to the resolution of the extinction data. Nevertheless, there are some differences seen at the scales of the cores, such as in Mu4 and Mu10. In Mu4, we have two peaked points, while only one is seen in theirs, and in Mu10 they have a plateau-like distribution with two peaks, while we have only one maximum.

To perform the spatial smoothing of the maps, we used the weighted mean method, which can introduce biases in the high-extinction regions (Ysard et al. 2013), leading to underestimates of the column density in the central regions of the cloud. Also, effects of small-scale cloud structure dominate the uncertainties in the extinction measurements (Lada et al. 1994) and can significantly bias the extinction maps toward low column densities (Lombardi 2009). However, as stated by Lombardi & Alves (2001) and Lombardi (2009), such biases can generally be ignored for very nearby clouds, which is the case of Musca.

Racca et al. (2009) showed that the NICE method applied to the 2MASS data is a reliable way to construct visual extinction maps, to obtain radial extinction profiles, and to analyze the stability of the cores. However, due to the sensitivity of the 2MASS data and the fact that the S/N of the NICE method is not as good for diffuse, low-extinction regions, the extinctions derived toward the center of the cores and the density contrast ($\xi_{\max}$) have to be seen as lower limits.

Although in exploring the regions of higher visual extinction we ensured that the S/N was greater than 3, to analyze the distribution of gas in the regions of visual extinction lower than 3 mag, also at high column densities, it is more appropriate to use the NICEST method, which is able to provide a good S/N and is less biased than the NICE and NICER (Lombardi & Alves 2001) methods.

4.2. Physical Properties of the Cores

4.2.1. Radial Density Profiles

The analyzed cores have different visual extinction peaks and radial extinction distributions, with steeper profiles that drop until they reach a relatively constant level of extinction between 7 and 9 mag. These extinction levels of the *plateau* are typical maxima extinctions estimated by star counts at optical wavelengths in some dark clouds (Cambrésy 1999).

From the Bonnor–Ebert fit we estimated that the surrounding cloud material exerts in the cores an external pressure ranging from 3×10^4 to 20×10^4 K cm^{-3}, which confines the cores to their present size and shape, with a radius that we estimated to be between 0.05 and 0.08 pc. The estimated pressures are similar to those estimated for other cores (Teixeira et al. 2005; Racca et al. 2009) and also of order of those estimated through predictions of the pressure-confined hydrostatic equilibrium model for the central region of Musca (Kainulainen et al. 2016).

4.2.2. Masses

The LTE masses of Mu4, Mu5, and Mu10 ($13.3 \pm 1.2\ M_\odot$, $21.2 \pm 1.5\ M_\odot$, and $31.6 \pm 2.6\ M_\odot$, respectively) are substantially larger than their Jeans mass ($9.3 \pm 3.2\ M_\odot$, $7.6 \pm 0.5\ M_\odot$, and $7.8 \pm 1.2\ M_\odot$, respectively). According to Larson (1978), condensations with LTE masses larger than their Jeans mass can further fragment and form more than one protostar. The extinction map of Mu4 (see Figure 6) suggests that it has fragmented into two cores, which we labeled as Mu4A and Mu4B, with similar extinction peaks.

The Bonnor–Ebert masses of the cores are $\sim 1\ M_\odot$, which is similar to what was found by Kandori et al. (2005), Teixeira et al. (2005), and Racca et al. (2009) for some cores, with and without YSOs associated.

4.2.3. Volumetric Density of Molecular Hydrogen

The mean central density of the cores that we have estimated from Bonnor–Ebert fits is $(5.6 \pm 2.3) \times 10^4$ cm^{-3}, which is in

agreement with values estimated for cores in other regions (Racca et al. 2009). Mu13 is the densest condensation of Musca. Its volumetric density, which we estimated from the NH_3 line, is $2.0 \times 10^4\,cm^{-3}$, which is typical of dense cores detected in NH_3 (Myers & Benson 1983; Benson & Myers 1989; Myers et al. 1991). The same parameter derived from the Bonnor–Ebert fit in Mu13 is $1 \times 10^5\,cm^{-3}$.

4.2.4. Kinetic Temperature

The kinetic temperature in Musca, which we estimated from ^{13}CO and $C^{18}O$ ($J = 1$–0) lines, ranges between 8 and 15 K, except in Mu4-1, where it was 52 K. The same range of temperatures is estimated from Bonnor–Ebert fits and is similar to what is observed in condensations of dark molecular clouds.

The mean kinetic temperature in Mu4 and Mu5 is 11 ± 2 K, which is equal to the dust temperature of these condensations obtained by Juvela et al. (2010), suggesting that the gas and dust in these condensations are thermalized (Lacy et al. 1994). When the gas becomes thermally coupled to the dust, it controls the temperature by its strongly temperature-dependent thermal emission, maintaining a low and almost constant temperature of about 10 K, which is an important feature of the star formation process, and makes possible the collapse of prestellar cores with small masses (Larson 2003), which is the case of Mu4 and Mu5.

The kinetic and excitation temperatures we estimated by NH_3 lines in Mu13 are 12 and 8 K, respectively. These values are similar to those obtained in cores of the Perseus molecular cloud complex (Ladd et al. 1994) and also in other cores in nearby dark clouds (Myers & Benson 1983). When the excitation temperature is smaller than the kinetic temperature, either the filling factor is smaller than 1 or "nonequilibrium conditions prevail" (Forster et al. 1987; Urquhart et al. 2015). Since the intensity ratio of the NH_3 hyperfine components ($\sim$0.3) suggests that Mu13 is in thermal equilibrium, the filling factor in this condensation should be smaller than 1.

4.2.5. Optical Depth

The $J = 1$–0 transition of $C^{18}O$ is optically thin in all observed positions, and the highest value is reached in Mu10-3 (0.35). The ^{13}CO optical depth is greater than 1 in some positions of Mu4, Mu5, and Mu10. It is approximately 2 in only one position observed in Mu10. Similar values were estimated by Vilas-Boas et al. (1994). However, Hacar et al. (2016) derived optical depths between 0.08 and 1.3 for $C^{18}O$ ($J = 2$–1) and between 0.5 and 9.5 for ^{13}CO ($J = 2$–1).

4.2.6. Radial Velocities and Line Profiles

We found that the radial velocity of the gas in Musca ranges from 2.9 to 4.0 $km\,s^{-1}$, with a systematic increase along the longer size of about $0.2\,km\,s^{-1}\,pc^{-1}$ from Mu4 to Mu13, similar to that found by Mizuno et al. (2001). Global velocity gradients of about 0.1 and $0.3\,km\,s^{-1}\,pc^{-1}$ are found by Vilas-Boas et al. (1994) and Hacar et al. (2016), respectively.

Almost all lines of ^{13}CO and $C^{18}O$ are symmetric, having Gaussian-like shapes, with mean line widths of $0.75 \pm 0.16\,km\,s^{-1}$ and $0.56 \pm 0.12\,km\,s^{-1}$, respectively. Studies of polarization along the filament of Musca show that the dispersion of the polarization angle in the north region of this cloud is high compared to other regions of the filament. The average of this parameter in the north region is $5\overset{\circ}{.}0 \pm 1\overset{\circ}{.}0$, while in the rest of the cloud it is $3\overset{\circ}{.}4 \pm 1\overset{\circ}{.}0$. Among 35 fields studied by Pereyra & Magalhães (2004) in Musca, one close to IRAS 12322-7023 has the highest dispersion of the polarization angle ($6\overset{\circ}{.}9$) observed in Musca. According to the theory of Chandrasekhar & Fermi (1953), we should have higher line widths in Mu13 than in other condensations. However, it is noticeable that Mu5 has the largest ^{13}CO line widths. The line widths of $C^{18}O$ do not show any tendency. In this sense, the line widths we observed in Musca do not show the same trend observed in the dispersion of the polarization angle, and they are not affected by the mechanism that produces the dispersion of the polarization angle observed by Pereyra & Magalhães (2004) in the field close to IRAS 12322-7023.

On the other side, the observed total velocity dispersion of ^{13}CO observed toward Mu13 ($0.41\,km\,s^{-1}$) is greater than in Mu10 ($0.26\,km\,s^{-1}$), is five times greater than in Mu5 ($0.08\,km\,s^{-1}$), and is eight times greater than observed in Mu4 ($0.05\,km\,s^{-1}$). This result reinforces the idea that the north part of the cloud is formed by the superposition of at least two independent clouds with different radial velocities, as shown by our integrated maps of ^{13}CO and $C^{18}O$ (see Figure 3). If these clouds have distinct magnetic field orientation, it is possible to explain the observed dispersion of the polarization angle in this region. Unfortunately, our data do not allow us to state whether these clouds are colliding and inducing star formation or are related to a physical process associated with the formation of the YSO. Observations of better tracers of dense regions with higher space resolution are still necessary to understand the gas distribution and the dynamical properties of Mu13 and other cores.

The line width of the hyperfine component of NH_3 in Mu13 is $0.71 \pm 0.03\,km\,s^{-1}$, which is similar to that obtained in other clouds (Ho et al. 1978) but is wider than in sources probed by Myers & Benson (1983). This NH_3 line width should be seen as an upper limit, since we did a Hanning smoothing of two channels in order to have a better S/N.

The nonthermal line widths for the mean molecular weight ($2.33\,m_H$) are $0.74 \pm 0.15\,km\,s^{-1}$ and are slightly larger than the thermal line widths derived from the estimated kinetic temperature ($0.45 \pm 0.03\,km\,s^{-1}$), suggesting that the observed line widths are dominated by nonthermal motions.

The estimated ratio σ_{NT}/σ_T ranges between 2 and 4, which suggests that the gas in the positions we have observed is in the transonic regime. Hacar et al. (2016), sampling positions along the main axis of the filament in ^{13}CO and $C^{18}O$ ($J = 2$–1) lines, concluded that the most internal region of Musca is subsonic. These results suggest that there is a cascade of the turbulence, from the transonic (outer regions) to subsonic regime (main axis of the filament). According to Larson (2003), the scale where there is a transition from supersonic to subsonic turbulence is 0.05–0.1 pc, which is approximately close to the dimension scales we obtained for the cores embedded in Musca ($\sim$0.07 pc).

4.2.7. Stability

Mu4, Mu5, and Mu10 have virial parameter $\alpha_{vir}(=M_V/M_{LTE}) \lesssim 1$. According to Bertoldi & McKee (1992), clouds in such a condition are virialized.

From the Bonnor–Ebert model, we estimated the stability parameters of the dense cores embedded in Musca to be between 4.5 and 5.7, indicating that the center-to-edge density

contrast is smaller than 14. This suggests that all cores are likely stable.

Mu13 is the unique condensation in Musca that contains a YSO, showing that it has faced instability. Its stability parameter is 4.6, one of the lowest observed in Musca. Unstable cores should have a stability parameter greater than 6.5 (Ebert 1955; Bonnor 1956), which was found in globules with evidence of active star formation by Harvey et al. (2001), Kandori et al. (2005), and Kainulainen et al. (2007). However, Racca et al. (2009) found that some globules with associated *IRAS* sources have stability parameters between 4.5 and 6.5. In their sample, only one globule with an associated *IRAS* source has a stability parameter greater than 6.5.

Analyzing the relation between the stability parameter and the Bonnor–Ebert temperature, Racca et al. (2009) found that the temperature decreases with increasing stability parameter. Unstable cores (three starless and one with an *IRAS* source) have $\xi_{\max} \sim 8.5$ and a Bonnor–Ebert temperature of 10 ± 3 K, and stable cores (eight starless and seven with an *IRAS* source) have $\xi_{\max} \sim 4.5$ and 15 ± 6 K. In our sample all cores are stable (one with an *IRAS* source and four starless), with stability parameters of 5.1 ± 0.5 and Bonnor–Ebert temperatures of about 8.8 ± 2.0 K. Even taking into account the uncertainty, our results do not follow the sample of cores observed by Racca et al. (2009), although our sample contains a small number of cores.

5. Conclusions

From the visual extinction map of Musca, constructed using NIR color excess of background stars extracted from the 2MASS PSC and the NICE method, we identified six dense cores with extinction peaks greater than 10 mag. We analyzed the stability of five of them, fitting their visual extinction radial profiles with a theoretical Bonnor–Ebert isothermal sphere model. One dense core is not well described by this model. We also estimated some physical properties of the gas toward these regions from visual extinction studies and also from emission lines of ^{13}CO ($J = 1$–0), C^{18}O ($J = 1$–0), and NH_3 ($J = K = 1$). The main conclusions of this work are as follows:

1. The fitted cores have stability parameters ranging between 4.5 and 5.7, showing that all of them are likely stable, including Mu13, which harbors an *IRAS* source.
2. The observed line widths range from ∼0.4 to 1.2 km s^{-1} and are dominated by nonthermal motions.
3. The derived range of Bonnor–Ebert temperature, from 7 to 13 K, agrees with the temperature range derived from ^{13}CO, C^{18}O, and NH_3 lines.
4. The Bonnor–Ebert masses of the cores range from 1.0 to 1.2 $M_\odot$. The averages of their radii and central volumetric densities are 0.07 pc and $\sim 5 \times 10^4$ cm^{-3}, respectively.
5. In Mu13, the observed ^{13}CO and C^{18}O lines show double peaks, whose integrated intensity maps suggest that these emissions come from distinct clouds overlapping along the line of sight.
6. The intensity ratio of the satellite to main hyperfine components of the NH_3 line toward Mu13 (∼0.3) suggests that this condensation is in thermal equilibrium.
7. The visual extinction (A_V), central volumetric density (n_c), and external pressure (P_{ext}) are highest in Mu13. However, other physical parameters do not show any tendency, suggesting that they are not sensitive to the evolutionary state. It is possible that A_V, n_c, and P_{ext} are the main parameters to explore in core candidates to form stars.

D.A.M. acknowledges the support of the Square Kilometer Array-South Africa (SKA-SA) postgraduate bursary initiative and the Coordenação de Aperfeiçoamento de Pessoal de Nível Superior (CAPES) doctoral fellowship. J.W.V.-B. acknowledges the support of the Fundação de Amaparo a Pesquisa de São Paulo (FAPESP) postdoctoral fellowship and the Smithsonian Astrophysical Observatory for support of a visiting scientist position. The authors would like to thank Dr. Paul Jaminet and the staff members of the SEST radio telescope and Dr. Gary Fuller and the staff members of the Parkes radio telescope, who made the observations used in this paper possible. This research was partially supported by a grant from the National Aeronautics and Space Administration (NASA) administrated by the American Astronomical Society.

Facilities: CTIO:2MASS, FLWO:2MASS, Parkes, SEST.

Software: DRAWSPEC, GILDAS.

References

Alves, J., Lada, C., & Lada, E. 2001, Msngr, 103, 1A
Andreazza, C. M., & Vilas-Boas, J. W. S. 1996, A&AS, 116, 21
Arnal, E. M., Morras, R., & Rizzo, J. R. 1993, MNRAS, 265, 1
Barrett, A. H., Ho, P. T. P., & Myers, P. C. 1977, ApJL, 211, L39
Benson, P. J., & Myers, P. C. 1989, ApJS, 71, 89
Bergin, E. A., Ciardi, D. R., Lada, C. J., et al. 2001, ApJ, 557, 209
Bertoldi, F., & McKee, C. F. 1992, ApJ, 395, 140
Bohlin, R. C., Savage, B. D., & Drake, J. F. 1978, ApJ, 224, 132
Bonnor, W. B. 1956, MNRAS, 116, 351B
Cambrésy, L. 1999, A&A, 345, 965
Caselli, P., Benson, P. J., Myers, P. C., et al. 2002, ApJ, 572, 238
Caselli, P., & Ceccarelli, C. 2012, A&ARv, 20, 56
Cernicharo, J., & Bachiller, R. 1984, A&AS, 58, 327
Chandrasekhar, S., & Fermi, E. 1953, ApJ, 118, 116
Corradi, W. J. B., Franco, G. A. P., & Knude, J. 1997, A&A, 326, 1215
Dickman, R. L. 1978a, AJ, 83, 363
Dickman, R. L. 1978b, ApJS, 37, 407
Ebert, R. 1955, ZA, 37, 217
Evans, N. J., II 1999, ARA&A, 37, 311
Feitzinger, J. V., & Stuewe, J. A. 1984, A&AS, 58, 365
Forster, J. R., Whiteoak, J. B., Gardner, F. F., et al. 1987, PASAu, 7, 189
Franco, G. A. P. 1991, A&A, 251, 581
Gardner, F. F., Whiteoak, J. B., Forster, J. R., et al. 1985, PASAu, 6, 176
Gregorio Hetem, J. C., Sanzovo, G. C., & Lepine, J. R. D. 1988, A&AS, 76, 347
Hacar, A., Kainulainen, J., Tafalla, M., et al. 2016, A&A, 587, A97
Harju, J., Walmsley, C. M., & Wouterloot, J. G. A. 1993, A&AS, 98, 51
Harvey, D. W. A., Wilner, D. J., Lada, C. J., et al. 2001, ApJ, 563, 903
Ho, P. T. P., Barrett, A. H., & Martin, R. N. 1978, ApJL, 221, L117
Ho, P. T. P., & Townes, C. H. 1983, ARA&A, 21, 239
Hollenbach, D. J., Werner, M. W., & Salpeter, E. E. 1971, ApJ, 163, 165
Huard, T. L., Myers, P. C., Murphy, D. C., et al. 2006, ApJ, 640, 391
Johnstone, D., Di Francesco, J., & Kirk, H. 2004, ApJ, 611, L45
Juvela, M., Ristorcelli, I., Montier, L. A., et al. 2010, A&A, 518, L93
Juvela, M., Ristorcelli, I., Pagani, L., et al. 2012, A&A, 541, A12
Juvela, M., Ristorcelli, I., Pelkonen, V. M., et al. 2011, A&A, 527, A111
Kainulainen, J., Beuther, H., Banerjee, R., et al. 2011, A&A, 530, A64
Kainulainen, J., Hacar, A., Alves, J., et al. 2016, A&A, 586, A27
Kainulainen, J., Lehtinen, K., Väisänen, P., et al. 2007, A&A, 463, 1029
Kandori, R., Nakajima, Y., Tamura, M., et al. 2005, AJ, 130, 2166
Knude, J., & Hog, E. 1998, A&A, 338, 897
Lacy, J. H., Knacke, R, Geballe, T. R., et al. 1994, ApJL, 428, L69
Lada, C. J., Lada, E. A., Clemens, D. P., et al. 1994, ApJ, 429, 694
Lada, C. J., Lombardi, M., & Alves, J. F. 2010, ApJ, 724, 687
Ladd, E. F., Myers, P. C., & Goodman, A. A. 1994, ApJ, 433, 117
Larson, R. B. 1978, MNRAS, 184, 69
Larson, R. B. 2003, RPPh, 66, 1651

Liszt, H. 2014, ApJ, 780, 10
Löhr, A., Bourke, T. L., Lane, A. P., et al. 2007, ApJS, 171, 478
Lombardi, M. 2009, A&A, 493, 735
Lombardi, M., & Alves, J. 2001, A&A, 377, 1023
Lu, X., Zhang, Q., Liu, H. B., et al. 2014, ApJ, 790, 84
Mangum, J. G., Wootten, A., & Mundy, L. G. 1992, ApJ, 388, 467
McKee, C. F., & Zweibel, E. G. 1992, ApJ, 399, 551
Mizuno, A., Hayakawa, T., Yamaguchi, N., et al. 1998, ApJ, 507, L83
Mizuno, A., Yamaguchi, R., Tachihara, K., et al. 2001, PASJ, 53, 1071
Myers, P. C. 1999, in Proc. 3rd Cologne-Zermatt Symp., The Physics and Chemistry of the Interstellar Medium, ed. V. Ossenkopf, J. Stutzki, & G. Winnewisser (Herdecke: GCA-Verlag), 227
Myers, P. C., & Benson, P. J. 1983, ApJ, 266, 309
Myers, P. C., Fuller, G. A., Goodman, A. A., et al. 1991, ApJ, 376, 361
Myers, P. C., Linke, R. A., & Benson, P. J. 1983, ApJ, 264, 517
Nielbock, M., & Chini, R. 2005, A&A, 434, 585
Pereyra, A., & Magalhães, A. M. 2004, ApJ, 603, 584
Racca, G., Gómez, M., & Kenyon, S. J. 2002, AJ, 124, 2178
Racca, G. A., Vilas-Boas, J. W. S., & de la Reza, R. 2009, ApJ, 703, 1444
Savage, B. D., & Mathis, J. S. 1979, ARA&A, 17, 73
Skrutskie, M. F., Cutri, R. M., Stiening, R., et al. 2006, AJ, 131, 1163
Tafalla, M., Myers, P. C., Caselli, P., et al. 2004, A&A, 416, 191
Teixeira, P. S., Lada, C. J., & Alves, J. F. 2005, ApJ, 629, 276
Urquhart, J. S., Figura, C. C., Moore, T. J. T., et al. 2015, MNRAS, 452, 4029
van Dishoeck, E. F., & Black, J. H. 1988, ApJ, 334, 771
van Dishoeck, E. F., Blake, G. A., Jansen, D. A., et al. 1995, ApJ, 447, 760
Vilas-Boas, J. W. S., Myers, P. C., & Fuller, G. A. 1994, ApJ, 433, 96
Vilas-Boas, J. W. S., Myers, P. C., & Fuller, G. A. 2000, ApJ, 532, 1038
Vuong, M. H., Montmerle, T., Grosso, N., et al. 2003, A&A, 408, 581
Walmsley, C. M., & Ungerechts, H. 1983, A&A, 122, 164
Whittet, D. C. B., Kirrane, T. M., Kilkenny, D., et al. 1987, MNRAS, 224, 497
Ysard, N., Abergel, A., Ristorcelli, I., et al. 2013, A&A, 559, A133